ACS OMEGA

http://pubs.acs.org/journal/acsodf

Article

Enhancing the Stability of Nicotine via Crystallization Using Enantiopure Tartaric Acid Salt Formers

Devin J. Angevine, Kristine Joy Camacho, Xiaotong Zhang, Javid Rzayev, and Jason B. Benedict*

Cite This: *ACS Omega* 2023, 8, 15535−15542

Read Online

ACCESS | Metrics & More | Article Recommendations | Supporting Information

ABSTRACT: Crystallization of nicotine, an oil prone to degradation at room temperature, has been demonstrated to be an effective means of creating nicotine-based materials with tunable thermal properties and improved resistance to photo-induced degradation. Herein, we show that both isomers of enantiomerically pure tartaric acid are highly effective salt formers when combined with nicotine. Both salts exhibit enhanced photostability, and with a melting point of 143.1 °C, the salt prepared using D-(−)-tartaric acid possesses one of the highest melting points for a crystalline nicotine solid reported to date.

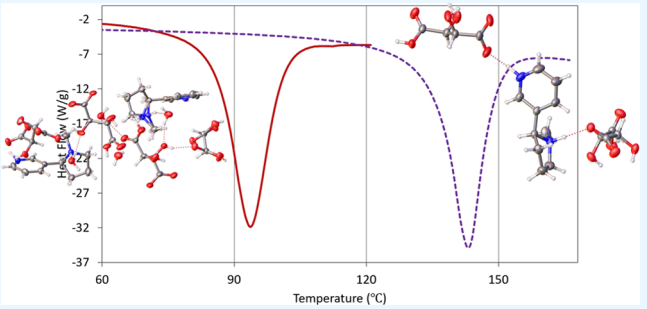

INTRODUCTION

Solid-state forms of active pharmaceutical ingredients (API) often possess enhanced stability relative to the liquid state.[1,2] The decreased stability can lead to shorter shelf lives and difficulties associated with their safe handling and storage. For example, propofol is a liquid anesthetic on the World Health Organization's (WHO's) list of essential medicine that is known to oxidize upon oxygen exposure.[3] As such, solid-state formulations utilizing crystal engineering have been explored as means of enhancing their stability and prolonging their shelf life.[4] Furthermore, Aakeröy et al. demonstrated that halogenated liquid chemicals can be stabilized in the solid state with improved properties using co-crystallization.[2] Additionally, the solid-state formulations, especially crystalline forms, provide a means of elucidating important noncovalent interactions in these materials through structure determination that can guide the design of future materials.

Nicotine, a widely consumed pharmacologically active substance, exhibits photo-induced degradation as well as degradation from ambient atmospheric air.[5] Under prolonged exposure to air or ultraviolet (UV) irradiation, pure nicotine decomposes into the primary components oxynicotine, nicotinic acid, and methylamine.[6] Conversion of the pure phase oil to the crystalline state provides a means of both tuning the thermal properties of the solid and enhancing the resistance to degradation.

Capucci et al. utilized crystal engineering principles to isolate and characterize three novel nicotine co-crystals.[7] This work demonstrated that nicotine can be isolated in the solid state with tunable properties such as melting point. While this was an important step forward to understanding and studying nicotine in solid forms, the synthesized nicotine co-crystals were created with halogenated and unsafe coformers, thus making them unsuitable for human consumption. As such it is necessary to utilize compounds that are suitable for human consumption to create nicotine solids through crystal engineering. Previous work has been done utilizing the family of malic acid compounds, orotic acid, and gentisic acid as such substances are listed as generally recognized as safe (GRAS) compounds by the U.S. Food and Drug Administration (FDA).[8−11] This work demonstrated a general approach for the creation of safer nicotine salts using GRAS-listed compounds.

Nicotinium bitartrate dihydrate is a commercially available nicotine salt used in many nicotine lozenges and pouches. This commercial material is produced using L-tartaric acid. Despite widespread use, the crystal structure and properties have not been reported. With the broader usage of these materials on the rise, herein, we report the synthesis and structural characterization of the nicotine crystallized with D-(−)- and L-(+)-tartaric acid (Scheme 1). Thermal characterization and photostability measurements on the nicotinium tartrate salts were measured to assess the performance of tartaric acid as a salt-forming agent relative to the previously reported salt formers.

EXPERIMENTAL SECTION

Materials. (*S*)-Nicotine (>95%) was acquired from TCI. L-(+)-Tartaric acid (99%) and D-(−)-tartaric acid (99%) were

Received: February 9, 2023
Accepted: April 5, 2023
Published: April 18, 2023

Scheme 1. Chemical Structures of the API Nicotine (Left) and the Salt Formers L-Tartaric Acid (Middle) and D-Tartaric Acid (Right)

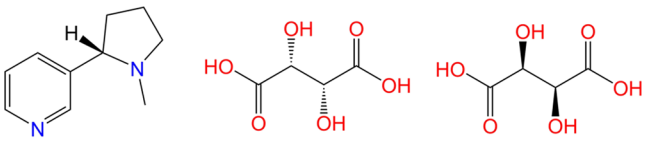

each purchased from Alfa Aesar. Ethanol (190 proof, USP-grade) and *n*-heptane were purchased from Decon Laboratories, Inc. and Fisher Scientific, respectively. Dimethyl sulfoxide-D_6 (D, 99.9%) and methanol-D_4 (D, 99.8%) were purchased from Cambridge Isotope Laboratories, Inc. Deionized (DI) water was obtained through the use of an in-house seven-stage reverse osmosis system.

Salt Synthesis. (*S*)-Nicotinium bis-L-(+)-tartrate dihydrate was synthesized using a modified slow evaporation setup. L-(+)-Tartaric acid (600.4 mg, 4.0 mmol) was added to a 20 mL scintillation vial with 10 mL of DI water and 10 mL of ethanol (190 proof). (*S*)-Nicotine (0.32 mL, 2.0 mmol) was added. The resulting solution was vortexed for 30 s at 3000 rpm on a VWR Mini Vortexer MV I. The solution was then stored in the dark uncapped to allow for crystal formation, while the solvent slowly evaporated. Once the solvent was about 90% evaporated, the crystalline product was collected via vacuum filtration and washed with *n*-heptane (3 × 5 mL) (694.7 mg, 69.69%). The yield was computed based on the formula weight of the L-tartrate salt (F.W. 498.4 g mol^{-1}).

(*S*)-Nicotinium bis-D-(−)-tartrate was synthesized using a modified slow evaporation setup. D-(−)-Tartaric acid (600.3 mg, 4.0 mmol) was added to a 200 mL tall beaker with 50 mL of ethanol (190 proof). (*S*)-Nicotine (0.32 mL, 2.0 mmol) was added. The resulting solution was vigorously stirred for 2 min. The solution was then stored in the dark uncapped to allow for crystal formation while the solvent slowly evaporated. Once the solvent was about 90% evaporated, the crystalline product was collected via vacuum filtration and washed with *n*-heptane (3 × 5 mL) (827.2 mg, 89.45%). The yield was computed based on the formula weight of the D-tartrate salt (F.W. 462.4 g mol^{-1}).

Single-Crystal X-ray Diffraction (SC-XRD). A Bruker SMART APEX-II CCD diffractometer installed at a rotating anode source (Mo Kα radiation, λ = 0.71073 Å) and equipped with an Oxford Cryosystems (Cryostream700) nitrogen gas-flow apparatus was used to collect single-crystal X-ray diffraction data. Five sets of data (360 frames each) were collected by the rotation method with 0.5° frame-width (ω scans) with 2.0 s exposure times for the single crystalline sample of (*S*)-nicotinium bis-L-(+)-tartrate dehydrate and 10.0 s exposure times for the single crystalline sample of the (*S*)-nicotinium bis-D-(−)-tartrate salt. Diffraction patterns obtained at low temperatures were of poor quality, potentially due to a low-temperature phase transition; thus, the data collections were performed at room temperature. Using Olex2, the structures were solved with intrinsic phasing via the ShelXT structure solution program and refined with the ShelXL software suite using least squares minimization.[12−14] Images of the structures were created using Olex2 and the Mercury 4.0 2021.2.0 visualization and analysis of crystal structures software suite.[15]

In the L-tartrate salt, atomic coordinates of H atoms attached to heteroatoms were freely refined with the exception of H11, H18, and H2A, which were placed geometrically (O−H = 0.82 Å; N−H = 0.98 Å). Difference contour mapping revealed density between O12 and O9 corresponding to a proton (H12A). This proton likely is shared between the two heteroatoms and has been modeled as such, resulting in the long bond level B alert during the checkCIF/PLATON report. Thermal parameters for H atoms attached to heteroatoms were constrained to be $U_{iso}(H) = 1.5U_{eq}(N)$ or $1.5U_{eq}(O)$. H atoms connected to carbon atoms were placed geometrically (C−H = 0.95 Å) and refined with thermal parameters constrained to be $U_{iso}(H) = 1.2U_{eq}(C)$. DFIX and DANG restraints were utilized in the L-tartrate salt to ensure chemically reasonable hydrogen-bonding geometries. Absolute configuration was assigned based upon the stereochemistry of the (*S*)-nicotine API. The Flack parameter was omitted in accordance with IUCr standards for reporting a structure when the absolute configuration is assigned based upon a known reference molecule.

In the D-tartrate salt, atomic coordinates of H atoms attached to heteroatoms were freely refined. Two q-peaks (0.37 and 0.26 e^{-} $Å^{-3}$) were located between O12 and O8, respectively. The peak located 0.896 Å from O12 was assigned as a proton and subsequently split with the second peak residing 0.933 Å from O8. This resulted in partial protonation of O12 [62(15) %] and O8 [38(15) %]. Thermal parameters for H atoms attached to heteroatoms were constrained to be $U_{iso}(H) = 1.5U_{eq}(N)$ or $1.5U_{eq}(O)$. H atoms connected to carbon atoms were placed geometrically (C−H = 0.95 Å) and refined with thermal parameters constrained to be $U_{iso}(H) = 1.2U_{eq}(C)$. Absolute configuration was assigned based on the stereochemistry of the API (*S*)-nicotine. The Flack parameter was removed in accordance with IUCr standards for reporting a structure in which the absolute configuration is assigned based on a known reference molecule, which in this structure is (*S*)-nicotine.

Crystal Melting Points. A Stuart SMP10 melting point apparatus was utilized to measure the melting point of the synthesized compounds. Four replicates were run for each salt.

Differential Scanning Calorimetry (DSC). A differential scanning calorimeter, model DSC Q200 (TA Instruments) was used to measure the thermal transitions of the sample. Approximately 10 mg of the synthesized compound was placed into an aluminum pan and sealed. The salt was scanned from 0 °C to above the melting point observed on the Stuart SMP10 at 20 °C min^{-1} under argon and nitrogen flow (10 mL min^{-1}. each) for two full cycles. Enthalpy of fusion was computed from the integrated area under the curve, and entropy of fusion was computed by applying Gibbs' free energy in accordance with equilibrium between the solid and liquid state being achieved at the fusion point.

UV Photodegradation. NMR analysis was done on a representative sample of the salt formers L-(+)-tartaric acid and D-(−)-tartaric acid, (*S*)-nicotine, and the synthesized (*S*)-nicotinium tartrate salts. Each sample was then irradiated with ultraviolet (UV) light in a home-built vented box with air flow for 24 h using four Southern New England Ultraviolet Company RPR-3000A UV bulbs (λ = 300 nm). NMR analysis was then carried out on each sample to screen for any UV photodegradation of products.

Nuclear Magnetic Resonance (NMR). NMR analysis was carried out using a Bruker NEO 400 MHz NMR spectrometer

https://doi.org/10.1021/acsomega.3c00849
ACS Omega 2023, 8, 15535−15542

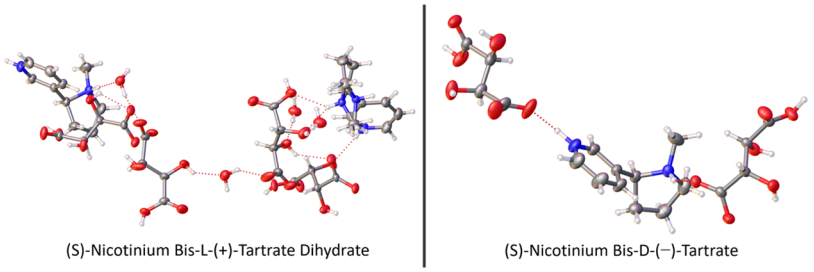

Figure 1. Asymmetric units of (*S*)-nicotinium bis-L-(+)-tartrate dihydrate (left) and (*S*)-nicotinium bis-D-(−)-tartrate (right). Atom colors: oxygen (red), nitrogen (blue), carbon (gray), hydrogen (white). Hydrogen-bonding interactions are depicted by red dashed lines.

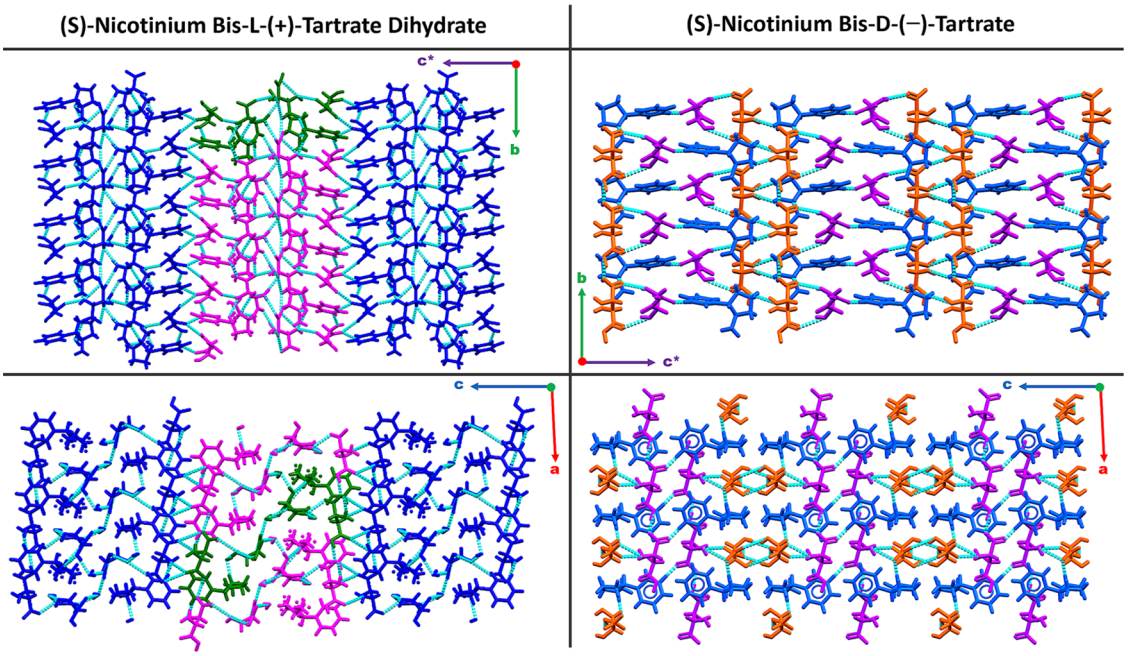

Figure 2. Crystal packing along [100] of L-tartrate salt (top left) and along [010] (bottom left). The asymmetric unit is highlighted in green, with columns of units shown in dark blue and opposing columns of units being rotated 180° about [010] highlighted in pink. Right column: Crystal packing viewed down [100] D-tartrate salt (top right) and down [010] (bottom right), which highlight the intermolecular hydrogen-bonding motifs. Infinite $C_1^1(7)$ chains running parallel to [010] are highlighted in orange, while infinite $C_1^1(7)$ chains running parallel to [100] are highlighted in purple. The nicotinium molecules (highlighted in blue) act as bridges between the chains. For all packing diagrams, hydrogen-bond interactions are highlighted with light blue dashed lines.

equipped with an iProbe and AutoTune assembly with variable temperature control, as well as a SampleCase autosampling unit. 80 transients were run for each sample. Appropriate deuterated solvents are labeled in each spectrum. Spectra were normalized to an intensity of 100.

Hirshfeld Surface Analysis. The Hirshfeld surface of each nicotinium tartrate salt was generated using *Crystal Explorer 17.5*.[16] For all salts, the d_{norm} surface was mapped using the color scale with the range −0.050 au (red) to 0.600 au (blue). In addition, two-dimensional (2D) fingerprint plots were generated as the outer nuclei (d_e) versus the inner nuclei (d_i) using an expanded interaction distance ranging from 0.6 to 2.8 Å.

Infrared (IR) Spectroscopy. Infrared spectral analysis was carried out on a PerkinElmer Spectrum Two FTIR spectrometer equipped with an attenuated total reflectance (ATR) module. Eight scans were averaged for each spectrum.

Powder X-ray Diffraction (PXRD). A Rigaku Ultima IV X-ray diffraction (XRD) System equipped with standard attachment (Cu Kα radiation, λ = 1.54 Å) was used to collect powder X-ray diffraction data. Over the 2θ range of 2−45° utilizing a 0.02° incremental step, data were collected utilizing a scanning speed of 5° per minute. Slit heights were set as follows: divergence slit: 2/3°; divergence height limiting slit: 10 mm; scattering slit: 2/3°; receiving slit: 0.3mm. Mercury 4.0 2021.2.0 visualization and analysis of crystal structures software suite was used to simulate PXRD patterns (Step: 0.02°, full width at half-maximum of 0.1°).[15] Maximum count values were normalized to 10,000 counts.

RESULTS AND DISCUSSION

Nicotinium Tartrate Salts Structural Characterization. Two nicotinium tartrate salts were synthesized; one utilizing D-(−)-tartaric acid and one utilizing L-(+)-tartaric acid. Single crystals of (*S*)-nicotinium bis-L-(+)-tartrate dihydrate (henceforth referred to as the L-tartrate salt) suitable for X-ray diffraction were obtained from slow evaporation of a water solution containing nicotine and L-tartaric acid in a 1:2 ratio, respectively. Similarly, single crystals of (*S*)-nicotinium bis-D-(−)-tartrate (henceforth referred to as the D-tartrate salt) were synthesized from slow evaporation from an ethanol solution containing a 1:2 ratio of nicotine to the salt former.

https://doi.org/10.1021/acsomega.3c00849
ACS Omega 2023, 8, 15535−15542

Table 1. Percentage of Each Interaction Type Present in Each API Nicotinium d_{norm} Surface That Was Computed for the Corresponding Tartrate Salt

interaction type	L-tartrate nondisordered	L-tartrate 63.3% of disorder	L-tartrate 36.7% of disorder	D-tartrate
O−H/H−O	41.2%	41.0%	40.6%	44.5%
O−C/C−O	3.4%	3.1%	3.3%	5.0%
O−N/N−O	0.8%	0.6%	0.6%	0.5%
H−H	46.9%	47.5%	47.8%	43.5%
H−C/C−H	5.8%	5.5%	5.5%	4.7%
H−N/N−H	1.1%	1.2%	1.2%	0.8%
C−C	0.7%	1.0%	0.9%	0.5%
C−N/N−C	0.1%	0.1%	0.1%	0.5%

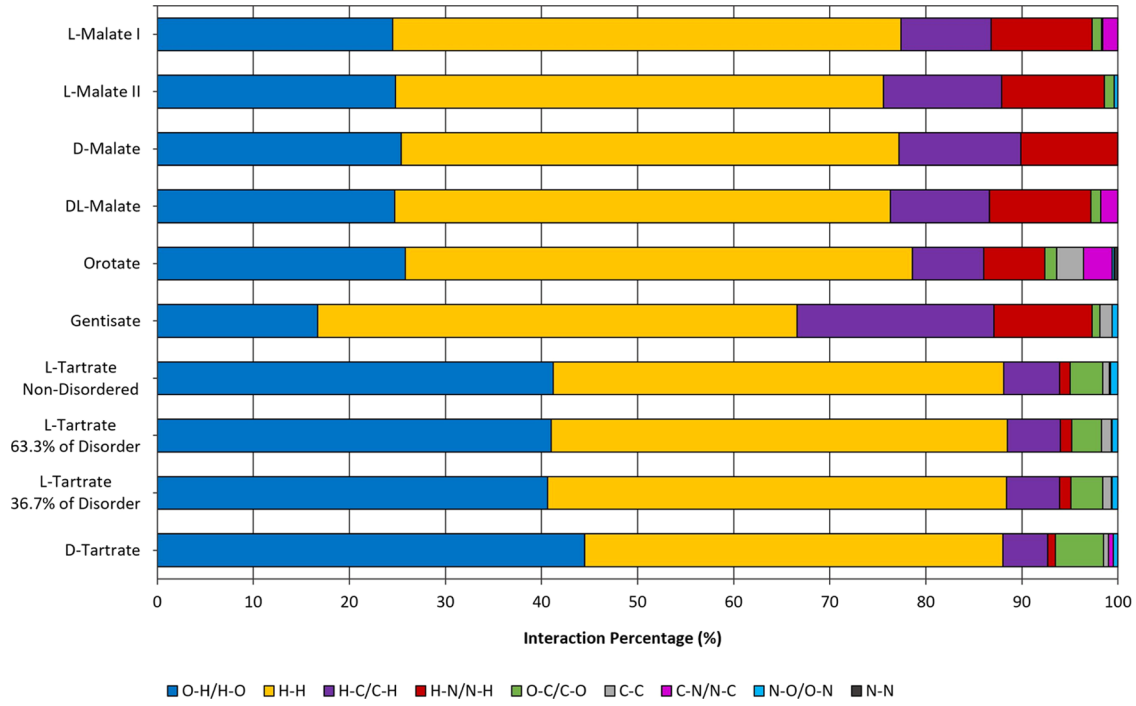

Figure 3. Interaction types and percentages for the API nicotinium of the tartrate salts compared with the orotate salt and the previously synthesized malate salts. *Crystal Explorer 17.5* was used to calculate Hirshfeld surfaces and percentages.

The asymmetric unit of the L-tartrate salt contains two nicotinium molecules, four tartrates, and four waters (Figure 1). Two doubly protonated nicotinium dications were charge-balanced with four L-tartrate monoanions. Protonated pyridinium groups interacted with an adjacent tartrate, while the major disordered species of the protonated methyl-pyrrolidinium group exhibited hydrogen-bonding interactions with neighboring water molecules. The minor component of the disordered methyl-pyrrolidinium moiety exhibits hydrogen bonding to a neighboring tartrate. Numerous discrete or D-type hydrogen-bonding interactions were observed throughout the asymmetric unit. Notable motifs were also observed including multiple $S(5)$ intramolecular interactions within tartrate molecules and $R_1^2(5)$ interaction motifs, which were observed between the disordered nicotinium and the nearest adjacent tartrate. It is of note that this ring-type motif is only observable when the disordered methyl-pyrrolidium resided in the more abundant conformation.

The L-tartrate salt bulk structure packs with asymmetric units stacking along [010] to form columns. These columns then pack along c^* with each adjacent column being rotated 180° about [010] (Figure 2). At the interface of the columns, an array of discrete hydrogen-bonding interactions intercalate to bind the columns together.

The nicotinium moieties of the D-tartrate salt were also observed to be doubly protonated. The D-tartrate salt has two discrete or D-type hydrogen-bonding interactions in the asymmetric unit. These interactions are between each of the nitrogens on the nicotinium and the tartrates. It was noted that the D-tartrate molecules each formed infinite $C_1^1(7)$ chains with adjacent tartrate molecules. Chains were observed as running parallel to [100], while the other series of chains ran parallel to [010] (Figure 2). The nicotinium molecules act as bridges between the chains along [100] and the chains along [010].

Hirshfeld Interaction Analysis and Comparison. Hirshfeld surface analysis provides a method for the quantification of a variety of intermolecular interaction properties such as the electrostatic potential or d_{norm} of a crystalline system.[17−19] Insight into these interactions and their relevance to the physical properties of the crystals provide a basis for the design of future system designs.

The interaction environment for the API (*S*)-nicotinium was analyzed for the L-tartrate salt and the D-tartrate salt utilizing d_{norm} surface mapping. The fingerprint plots are provided in the Supporting Information. The interactions were then

https://doi.org/10.1021/acsomega.3c00849
ACS Omega 2023, 8, 15535−15542

compared to (*S*)-nicotinium interaction environments from the previously reported malate and orotate salts.

The L-tartrate salt surface was generated for the nondisordered nicotinium, as well as one for each of the possible occupancies of the disordered nicotinium molecule that was present in the asymmetric unit (three in total). As observed in Table 1, when the L-tartrate salt API environments are examined, we find that within the disorder, the more abundant conformation possessed slightly more O−H/H−O-type interactions (41.0 vs 40.6%) and 0.1% more C−C interactions. This conformation also has slightly fewer H−H interactions and fewer O−C/C−O-type interactions. The nondisordered nicotinium had more O−H/H−O interactions, more O−C/C−O interactions, more O−N/N−O interactions, and more H−C/C−H-type interactions than either conformation of the disordered nicotinium had. The nondisordered nicotinium also had 0.1% fewer H−N/N−H interactions and fewer C−C-type interactions.

In comparison to the L-tartrate salt, the D-tartrate salt possessed significantly more O−H/H−O-type interactions and more C−N/N−C- and O−C/C−O-type interactions. Significantly fewer H−H interactions are observed along with slightly fewer C−C-, O−N/N−O-, H−N/N−H-, and H−C/C−H-type interactions. Overall, the same eight types of interactions were observed in all computed surfaces for both the L-tartrate salt and the D-tartrate salt. Also of note is that the four most abundant interaction types (H−H, H−O/O−H, H−C/C−H, and O−C/C−O) were conserved across all of the tartrate salts.

The nicotinium interactions found in the tartrate salts were then compared to the API interactions previously reported for the nicotinium malate salts, nicotinium gentisate salt, and nicotinium orotate salt (Figure 3). Interestingly, the tartrate salts described herein had significantly more H−O/O−H interactions than any of the malate salts or the gentisate and orotate salt, likely due in part to the additional hydroxyl groups present in the tartaric acid salt former in contrast to the orotic acid and malic acid salt formers used in the orotate and malate salts, respectively. The tartrates also had nearly half the percentages of H−C/C−H interactions in comparison to the previously reported salts. The tartrates also had about one-tenth of the H−N/N−H interactions in comparison to the malate salts. Like the gentisate and malate salts, the tartrate salts exhibited no N−N-type interactions, leaving only the orotate salt possessing this unique interaction type. The percentage of O−C/C−O interactions present in the L-tartrate surfaces was about 3 times higher than those found in the malate, gentisate, and orotate salts, with the exception of the D-malate, which possessed no interactions of this type. This demonstrates that while the O−C/C−O interactions are a relatively small percentage across all systems, they contribute slightly more in each tartrate salt relative to the other solids compared herein. Relatively small percentages of C−C interactions were present across all computed tartrate surfaces similar to the gentisate and orotate salts, which possessed C−C interactions at a slightly higher abundance.

Thermal Characterization. Understanding the thermal behavior of the crystalline solids can prove useful in the design and engineering of future materials.[20−22] Salt melting points, initially determined utilizing a Stuart SMP10 digital melting point apparatus, were determined to be 90−93 °C for the L-tartrate salt and 139−144 °C for the D-tartrate salt. Differential scanning calorimetry (DSC) based on these melting points was performed on a sample of each tartrate salt. Each sample was cycled twice with the heating cycles of the first scan of each tartrate salt shown in Figure 4, and the associated thermal

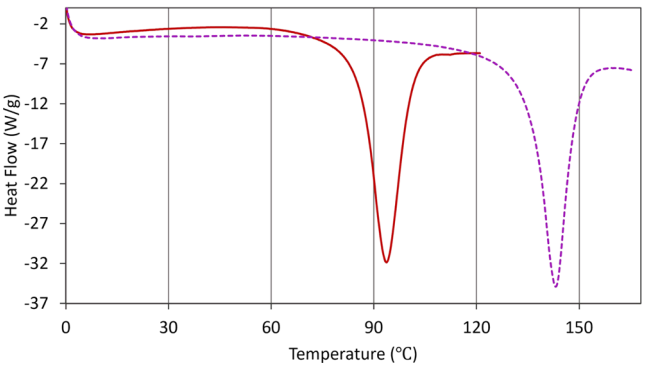

Figure 4. DSC scans (exo-up) showing the endotherms from the heating cycles of the first scan for L-tartrate (solid red line) and D-tartrate (dashed purple line).

properties are listed in Table 2. No evidence for a recrystallization event was observed for either salt during the second scan indicating the salts melted into an amorphous material as observed for other nicotine salts.[8−10] The full two-cycle DSC scans for each tartrate salt with exothermic transition having a positive heat flow are present in Figures S5 and S6.

The L-tartrate salt exhibited a sharp endothermic peak associated with melting at 93.7 °C. This thermal event was accompanied by an enthalpy of fusion ($\Delta H^{\circ}_{fusion}$) of 50.89 kJ mol^{-1} and an entropy of fusion ($\Delta S^{\circ}_{fusion}$) of 13.899 × 10^{-2} kJ mol^{-1} K^{-1}. Likewise, the D-tartrate salt exhibited a sharp endothermic peak associated with melting at 143.1 °C. This melting event was accompanied by an $\Delta H^{\circ}_{fusion}$ value of 38.55 kJ mol^{-1} and an $\Delta S^{\circ}_{fusion}$ value of 9.261 × 10^{-2} kJ mol^{-1} K^{-1}.

Compared to the other nicotine salts that have been reported, the L-tartrate salt represents the second-lowest-melting-point nicotine salt, with the nicotinium D-malate salt possessing a 0.3 °C lower melting point as indicated via DSC. However, the L-tartrate salt exhibits the largest $\Delta H^{\circ}_{fusion}$ and $\Delta S^{\circ}_{fusion}$ values of any reported nicotine-containing solid. The D-tartrate salt represents the second-highest-melting nicotine-containing solid that has been reported. The previously reported nicotinium orotate hemihydrate possesses a melting point of 135.5 °C while the D-tartrate salt melts 7.6 °C higher at 143.1 °C, thus making it the highest-melting nicotine salt reported in the literature. Both of the nicotinium tartrate salts offer enhanced thermal stability and higher melting points over any of the reported nicotine co-crystals, much like all other nicotine salts that have been reported.

The salt melting points were compared to the tartaric acid melting point (T_m), the difference being ΔT_m. This measure of performance was reported previously for the nicotinium malate and orotate salts and the halogenated nicotine co-crystals by Capucci et al. As the salt former tartaric acid possesses a melting point of 170.2 °C, this leads to a 76.5 °C value for ΔT_m for the L-tartrate salt and a 27.1 °C ΔT_m value for the D-tartrate salt.[23] The nicotinium malate salts exhibited ΔT_m values ranging from 5.4 to 34.2 °C, while the halogenated nicotine co-crystals were shown to possess a ΔT_m range of 55−78 °C. The gentisate salt had a ΔT_m value of 42.7 °C, while the nicotinium orotate hemihydrate salt possessed a far greater

https://doi.org/10.1021/acsomega.3c00849
ACS Omega 2023, 8, 15535−15542

Table 2. Thermodynamic Properties of the L-Tartrate Salt and D-Tartrate Salt from DSC

salt	Stuart SMP10 melting point (°C)	DSC endotherm melting point (°C)	$\Delta H^{\circ}_{fusion}$ (J g^{-1})	$\Delta H^{\circ}_{fusion}$ (kJ mol^{-1})	$\Delta S^{\circ}_{fusion}$ (kJ mol^{-1} K^{-1})
(*S*)-nicotinium bis-L-(+)-tartrate dihydrate	90−93	93.7	102.10	50.89	13.899×10^{-2}
(*S*)-nicotinium bis-D-(−)-tartrate	139−144	143.1	83.37	38.55	9.261×10^{-2}

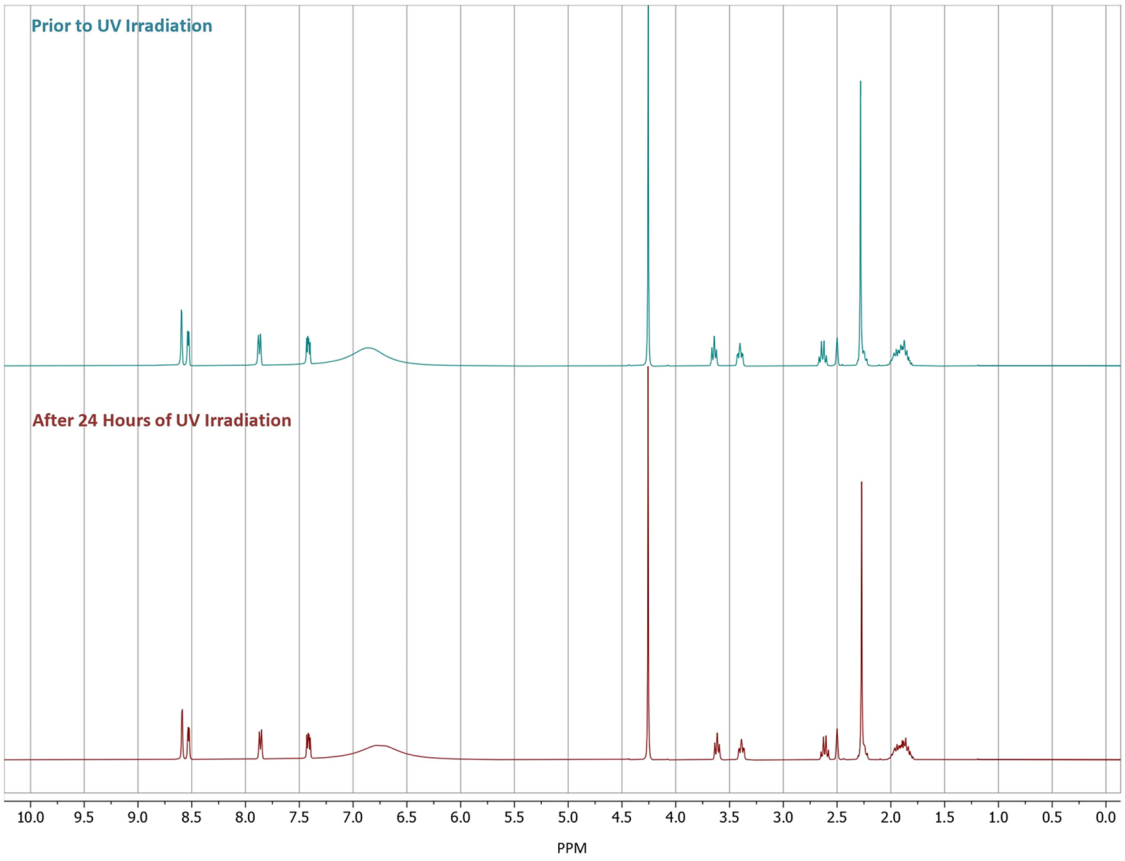

Figure 5. ^{1}H NMR spectra of dimethyl sulfoxide (DMSO) solutions of L-tartrate dihydrate prepared from samples in which the crystalline phase received either no UV irradiation (upper) or 24 h of UV irradiation (lower).

ΔT_m value of 215.4 °C. Thus, the D-tartrate salt ΔT_m value resides within the range of the malate salts, while the L-tartrate salt ΔT_m value resides within the ΔT_m range of the halogenated nicotine co-crystal values.

UV Photodegradation Testing. Pure nicotine is known to exhibit a range of sensitivities including air, moisture, and light which contribute to the degradation of the API.[5,6] Despite the fact that nicotine degradation pathways are not well studied, it is known that degradation products such as oxidized nicotine, methylamine, and nicotinic acid may form as a result of exposure to ultraviolet (UV) irradiation.[24] Crystalline forms of nicotine may offer the ability to curb degradation by restricting the quantity of molecular oxygen that can diffuse through the material. Thus, crystal engineering provides a means of stabilizing and effectively limiting UV-induced degradation of the API nicotine. By improving the stability of nicotine under ambient conditions, the shelf life and storage conditions of this API may be improved.

The photostability of each of the synthesized nicotinium tartrate salts was analyzed by irradiating a sample of each in a UV photoreactor for 24 h. After the irradiation period, a representative portion of the sample (10 mg) was analyzed via ^{1}H NMR spectroscopy. The extent of UV-irradiation-induced damage was assessed by comparing the spectrum of each sample prior to irradiation to the spectrum acquired after UV irradiation. In addition to the salts, the pure API as well as each salt former were analyzed before and after 24 h of irradiation as controls for this series of experiments.

Each of the salt formers, L-tartaric acid and D-tartaric acid, showed no detectable degradation in the post-UV irradiation spectra compared to the spectra acquired prior to irradiation. In contrast to this, the pure API (*S*)-nicotine exhibited numerous new peaks in the spectrum after irradiation, thereby confirming that the neat API does undergo UV-light-induced degradation. Like the salt formers, both the nicotinium L-tartrate salt (Figure 5) and the nicotinium D-tartrate salt (Figure S15) exhibited no degradation in the post-irradiation spectra. This is much the same as previously reported nicotinium orotate and nicotinium malate salts, thus further substantiating that crystalline forms of nicotine offer an approach to isolate photostable nicotine materials.[8,10]

CONCLUSIONS

Enantiomerically pure tartaric acid has been demonstrated to be a highly effective salt former when combined with nicotine. Unsurprisingly, both salts exhibit extensive hydrogen bonding

https://doi.org/10.1021/acsomega.3c00849
ACS Omega 2023, 8, 15535−15542

within their respective lattices, undoubtedly due to the large number of donors and acceptors found in both components.

Despite the presence of similar interaction environments determined through the analysis of the Hirschfeld surfaces, the salts possessed remarkably different thermal properties. While the L-tartrate salt melts at a modest 93.7 °C, the D-tartrate salt melts at 143.1 °C, one of the highest melting points for a crystalline nicotine solid reported to date.

Similar to other reported nicotine salts, neither nicotinium tartrate salt reported herein exhibited any detectable photodegradation upon prolonged exposure to UV irradiation, which further supports the claim that the crystallization of nicotine is an effective means of creating nicotine-based materials with improved resistance to photo-induced degradation. Further, the ability to synthesize these materials utilizing GRAS compounds demonstrates the feasibility of this approach to the design of safer nicotine-based materials through crystal engineering.

■ ASSOCIATED CONTENT

Supporting Information

The Supporting Information is available free of charge at https://pubs.acs.org/doi/10.1021/acsomega.3c00849.

Crystallographic data (CIF)

Crystallographic data (CIF)

Previously reported nicotine solids; crystallographic information; structural data deposition; (*S*)-nicotinium bis-L-(+)-tartrate dihydrate crystals and crystal structure data; (*S*)-nicotinium bis-D-(−)-tartrate crystals and crystal structure data; carbon−oxygen bond lengths for tartrate carboxyl groups; DSC scans; UV degradation study diagram and spectra; infrared (IR) spectra; nicotinium tartrate salts Hirshfeld fingerprint plots; and powder X-ray diffraction patterns (PDF)

■ AUTHOR INFORMATION

Corresponding Author

Jason B. Benedict − *Department of Chemistry, University at Buffalo, Buffalo, New York 14260-3000, United States;* orcid.org/0000-0002-8992-7165; Email: jbb6@buffalo.edu

Authors

Devin J. Angevine − *Department of Chemistry, University at Buffalo, Buffalo, New York 14260-3000, United States*

Kristine Joy Camacho − *Department of Chemistry, University at Buffalo, Buffalo, New York 14260-3000, United States*

Xiaotong Zhang − *Department of Chemistry, University at Buffalo, Buffalo, New York 14260-3000, United States*

Javid Rzayev − *Department of Chemistry, University at Buffalo, Buffalo, New York 14260-3000, United States;* orcid.org/0000-0002-9280-1811

Complete contact information is available at: https://pubs.acs.org/10.1021/acsomega.3c00849

Author Contributions

The authors declare no conflict of interest. The final version of this manuscript was approved by all authors. Data curation: D.J.A., K.J.C., X.Z., and J.R.; Formal analysis: D.J.A.; Funding acquisition: J.B.B.; Project administration: J.B.B.; Writing—original draft: D.J.A.; Writing—review & editing: D.J.A., J.R., and J.B.B.

Notes

The authors declare no competing financial interest.

■ ACKNOWLEDGMENTS

Funding for D.J.A., X.Z., and J.B.B. was provided by: National Science Foundation, Directorate for Mathematical and Physical Sciences (award no. DMR-2003932).

■ REFERENCES

(1) Morissette, S. L.; Almarsson, O.; Peterson, M. L.; Remenar, J. F.; Read, M. J.; Lemmo, A. V.; Ellis, S.; Cima, M. J.; Gardner, C. R. High-throughput crystallization: polymorphs, salts, co-crystals and solvates of pharmaceutical solids. *Adv. Drug Delivery Rev.* **2004**, *56*, 275−300.

(2) Aakeröy, C. B.; Wijethunga, T. K.; Benton, J.; Desper, J. Stabilizing volatile liquid chemicals using co-crystallization. *Chem. Commun.* **2015**, *51*, 2425−2428.

(3) Baker, M. T.; Naguib, M.; Warltier, D. C. Propofol: The Challenges of Formulation. *Anesthesiology* **2005**, *103*, 860−876.

(4) Bacchi, A.; Capucci, D.; Giannetto, M.; Mattarozzi, M.; Pelagatti, P.; Rodriguez-Hornedo, N.; Rubini, K.; Sala, A. Turning Liquid Propofol into Solid (without Freezing It): Thermodynamic Characterization of Pharmaceutical Cocrystals Built with a Liquid Drug. *Cryst. Growth Des.* **2016**, *16*, 6547−6555.

(5) Adamek, E.; Goniewicz, M.; Baran, W.; Sobczak, A. The Study on the Photocatalytic Degradation of Nicotine. *Chem* **2015**, *2015*, No. 157781.

(6) Rayburn, C. H.; Harlan, W. R.; Hanmer, H. R. The Effect of Ultraviolet Radiation on Nicotine. *J. Am. Chem. Soc.* **1941**, *63*, 115−116.

(7) Capucci, D.; Balestri, D.; Mazzeo, P. P.; Pelagatti, P.; Rubini, K.; Bacchi, A. Liquid Nicotine Tamed in Solid Forms by Cocrystallization. *Cryst. Growth Des.* **2017**, *17*, 4958−4964.

(8) Angevine, D. J.; Camacho, K. J.; Rzayev, J.; Benedict, J. B. Nicotine Refined: Crystal Engineering of (S)-Nicotinium Malate Salts. *Cryst. Growth Des.* **2022**, *22*, 1594−1603.

(9) Benedict, J. B.; Angevine, D. J. Nicotine Materials, Methods of Making Same, and Uses Thereof. WO Patent WO2021126313A12022.

(10) Angevine, D. J.; Camacho, K. J.; Rzayev, J.; Benedict, J. B. Transforming liquid nicotine into a stable solid through crystallization with orotic acid. *CrystEngComm* **2022**, *24*, 6155−6164.

(11) Angevine, D. J.; Camacho, K. J.; Rzayev, J.; Benedict, J. B. Enhancing the Photo and Thermal Stability of Nicotine through Crystal Engineering with Gentisic Acid. *Molecules* **2022**, *27*, 6853.

(12) Sheldrick, G. M. SHELXT-Integrated space-group and crystal-structure determination. *Acta Crystallogr., Sect. A: Found. Adv.* **2015**, *71*, 3−8.

(13) Sheldrick, G. M. Crystal structure refinement with SHELXL. *Acta Crystallogr., Sect. C: Cryst. Struct. Commun.* **2015**, *71*, 3−8.

(14) Dolomanov, O. V.; Bourhis, L. J.; Gildea, R. J.; Howard, J. A. K.; Puschmann, H. OLEX2: a complete structure solution, refinement and analysis program. *J. Appl. Crystallogr.* **2009**, *42*, 339−341.

(15) Macrae, C. F.; Sovago, I.; Cottrell, S. J.; Galek, P. T. A.; McCabe, P.; Pidcock, E.; Platings, M.; Shields, G. P.; Stevens, J. S.; Towler, M.; Wood, P. A. Mercury 4.0: from visualization to analysis, design and prediction. *J. Appl. Crystallogr.* **2020**, *53*, 226−235.

(16) Spackman, P. R.; Turner, M. J.; McKinnon, J. J.; Wolff, S. K.; Grimwood, D. J.; Jayatilaka, D.; Spackman, M. A. CrystalExplorer: a program for Hirshfeld surface analysis, visualization and quantitative analysis of molecular crystals. *J. Appl. Crystallogr.* **2021**, *54*, 1006−1011.

(17) Alvarez-Lorenzo, C.; Castiñeiras, A.; Frontera, A.; García-Santos, I.; González-Pérez, J. M.; Niclós-Gutiérrez, J.; Rodríguez-González, I.; Vílchez-Rodríguez, E.; Zaręba, J. K. Recurrent motifs in pharmaceutical cocrystals involving glycolic acid: X-ray characterization, Hirshfeld surface analysis and DFT calculations. *CrystEngComm* **2020**, *22*, 6674−6689.

(18) Sharfalddin, A.; Davaasuren, B.; Emwas, A.-H.; Jaremko, M.; Jaremko, Ł.; Hussien, M. Single crystal, Hirshfeld surface and theoretical analysis of methyl 4-hydroxybenzoate, a common cosmetic, drug and food preservative—Experiment versus theory. *PLoS One* **2020**, *15*, No. e0239200.
(19) Al-Wahaibi, L. H.; Joubert, J.; Blacque, O.; Al-Shaalan, N. H.; El-Emam, A. A. Crystal structure, Hirshfeld surface analysis and DFT studies of 5-(adamantan-1-yl)-3-[(4-chlorobenzyl)sulfanyl]-4-methyl-4H-1,2,4-triazole, a potential 11β-HSD1 inhibitor. *Sci. Rep.* **2019**, *9*, No. 19745.
(20) Perlovich, G. L. Thermodynamic characteristics of cocrystal formation and melting points for rational design of pharmaceutical two-component systems. *CrystEngComm* **2015**, *17*, 7019−7028.
(21) Perlovich, G. L. Two-component molecular crystals: evaluation of the formation thermodynamics based on melting points and sublimation data. *CrystEngComm* **2017**, *19*, 2870−2883.
(22) Perlovich, G. Melting points of one- and two-component molecular crystals as effective characteristics for rational design of pharmaceutical systems. *Acta Crystallogr., Sect. B: Struct. Sci., Cryst. Eng. Mater.* **2020**, *76*, 696−706.
(23) Wang, X.; Zhang, X.; Black, S.; Dang, L.; Wei, H. Solid−Liquid Equilibrium of d- and l-Tartaric Acid and Their Importance for Enantioseparation. *J. Chem. Eng. Data* **2012**, *57*, 1779−1786.
(24) Henry, T. A. *The Plant Alkaloids*, 4th ed.; Churchill, 1949; pp 36−43.

https://doi.org/10.1021/acsomega.3c00849
ACS Omega 2023, 8, 15535−15542